

Imaging Pulsed Laser Deposition oxide growth by in-situ Atomic Force Microscopy

W.A. Wessels, T.R.J. Bollmann,^{a)} D. Post, G. Koster, and G. Rijnders

University of Twente, Inorganic Materials Science, MESA⁺ Institute for Nanotechnology, P.O. Box 217, NL-7500AE Enschede, The Netherlands

(Dated: 1 March 2022)

To visualize the topography of thin oxide films during growth, thereby enabling to study its growth behavior quasi real-time, we have designed and integrated an atomic force microscope (AFM) in a pulsed laser deposition (PLD) vacuum setup. The AFM scanner and PLD target are integrated in a single support frame, combined with a fast sample transfer method, such that in-situ microscopy can be utilized after subsequent deposition pulses. The in-situ microscope can be operated from room temperature (RT) up to 700°C and at (process) pressures ranging from the vacuum base pressure of 10^{-6} mbar up to 1 mbar, typical PLD conditions for the growth of oxide films. The performance of this instrument is demonstrated by resolving unit cell height surface steps and surface topography under typical oxide PLD growth conditions.

I. INTRODUCTION

A fascinating material class are the perovskite oxides due to their wealth in physical properties such as superconductivity, ferromagnetism, ferro- and dielectricity¹. Induced by the discovery of high- T_C superconductors, pulsed laser deposition (PLD) has become a popular thin film growth technique to fabricate high quality oxide materials^{2,3}. The strength of depositing complex oxides with PLD comes from the fact that relative high oxygen pressures can be used while still having high kinetic energy ablated species, which strongly influences the films properties. Development of the current *in-situ* diagnostic tools such as high-pressure reflection high-energy electron diffraction (RHEED)⁴, surface x-ray diffraction (SXRD)⁵ and the more rarely used optical spectroscopic ellipsometry (SE), enabled to observe *in operando* the oxide thin film growth. Using RHEED e.g., the growth mode and in some conditions the number of grown unit cells can be deduced by measuring the step density over time⁶⁻⁸. The specular rod in SXRD describes layer filling when the diffuse scattering contains information about the spatial distribution of islands, whereas with SE the evolution of the electronic structure can be monitored during film growth^{9,10}. Although these scattering techniques are well established tools for monitoring the growth of oxides *in operando*, the reciprocal information contained can be hard to interpret and they do not allow to probe growth properties of individual thin film islands as the surface reflectivity signal typically probes and averages over a surface area of millimeters in size. Besides this, diffraction techniques typically require crystalline surface planes to enable observation at all.

For microscopic real-space observations a popular diagnostic tool available are the scanning probe microscopes (SPM), enabling monitoring the surface topology at the (sub)nanometer spatial resolution¹¹⁻¹⁴. As most perovskite oxides are insulators or have a large band gap,

application of scanning tunneling microscopy (STM) is rather limited as it is based on a tunneling current flowing between sample and tip^{15,16}. Within the field of (PLD) oxide growth, microscopy analysis on surfaces is therefore typically done by post-deposition *ex-situ* atomic force microscopy (AFM) or by *in-situ* ultra high vacuum (UHV) AFM. However, microscopically probing the surface during deposition is however a prerequisite in order to broaden our understanding of thin oxide film growth. Real space microscopy during film growth would give complementary information besides reciprocal techniques about microscopic events in thin film growth such as diffusion processes, ripening, defect formation etc. by measuring the nucleation density and individual thin film island evolution over time in between subsequent deposition pulses¹⁷, as in PLD deposition and growth are separated in time.

A first design and demonstration of a conventional AFM operating at metal-oxide PLD conditions has been reported^{18,19}, however the main drawback of typical AFM is the low sample throughput, as *in-operando* monitoring requires high-speed AFM instrumentation. Conventional AFMs are slow due to the low bandwidth of the cantilever, AFM scanner and electronics and optical detection signal. Recently, a lot of progress has been made to increase the bandwidth of these components in different environments, which shows the potential of high speed AFM in PLD conditions²⁰⁻²⁴.

Here, we present the concept, specifications, design and performance of an atomic force microscope (AFM) in a pulsed laser deposition (PLD) vacuum setup. The setup consists of an in-situ AFM joined in an aluminum frame with an in geometrically position separated PLD position. Combined with a fast sample transfer system, this enables in-situ microscopy after subsequent deposition pulses. The AFM has been developed such that tapping mode (TM) and frequency modulated (FM) AFM can be applied at typical PLD conditions ranging from room temperature (RT) up to 700°C and at (process) pressures ranging from the vacuum base pressure of 10^{-6} mbar up to 1 mbar. The performance of this instrument is demonstrated by resolving unit cell height steps of a

^{a)}Electronic mail: t.r.j.bollmann@utwente.nl

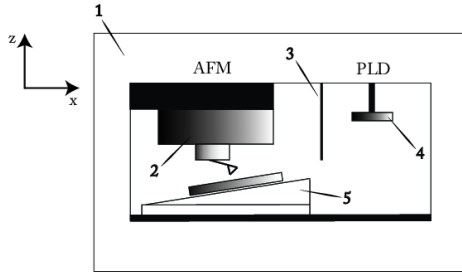


FIG. 1. Conceptual drawing of the PLD setup combined with *in-situ* AFM. Imaging and deposition are geometrically in position separated to prevent hindering of deposition and tip contamination. A fast transfer stage is moving the sample back and forth between imaging and deposition position. 1) support frame, 2) AFM scanner, 3) plasma screen, 4) PLD target and 5) sample/heater transfer stage.

SrTiO₃(001) surface at PLD conditions as well as the evolution of the surface topography of a grown BiFeO₃ film, a prototypical perovskite film. We conclude this paper with an outlook towards future applications as well as limitations of the current design.

II. CONCEPT

Fig. 1 shows a schematic illustration of a concept of AFM during PLD. In a support frame, an AFM scanner and PLD target are installed and a sample transfer stage is included. The AFM scanner is positioned geometrically separated from the PLD position for a main reason: It prevents blocking of deposition on the as-grown surface and unwanted AFM tip contamination. As deposition and growth in PLD are separated in time, growth can be studied in between subsequent pulses using this concept. A plasma screen between AFM and PLD should prevent any PLD plasma contamination on the AFM scanner.

In this concept, a sample is transferred back and forth between AFM and PLD, where the sample transfer is based on linear motion, see Fig. 1. A sample heater is mounted on top of a linear motion slider. The concept is such that the side approach²⁵ can be applied to reduce the time delay between PLD and AFM monitoring of the sample surface. The proposed configuration is straightforward to combine PLD with other diagnostics tools, such as scattering techniques as RHEED and plasma diagnostic tools for an increased understanding of thin film growth in PLD.

III. SPECIFICATIONS

To image the surface topography at PLD conditions, the AFM has to be operated at pressures ranging from 10^{-6} mbar up to process pressures of 10^{-1} mbar. The applied gases typically involve (a mixture of) oxygen, argon and/or nitrogen.

The temperature window of typical growth conditions runs from room temperature (RT) up to about 700°C,

where the exact substrate temperature depends on the substrate material and ablated species.

AFM imaging, resolving the growth properties of individual thin film islands requires a stable AFM imaging at an image size of about $1 \times 1 \mu\text{m}^2$. A short mechanical loop between the to be imaged substrate and AFM cantilever is required such that the noise levels, both, electronic and vibrational, should not exceed the substrate stepheight, typical <0.4 nm as typical oxide substrate steps are around 0.4 nm in height. This resolution is required both out-of-plane and in-plane.

To suppress thermal drift, an effective temperature stabilization is required. A thermal drift out-of-plane and in-plane, which enables measurement during 1 h would be required, as it is a typically duration involved in a PLD experiment. As we want to make use of image sizes of about $1 \times 1 \mu\text{m}^2$, this requires any in-plane drift to stay below 50 nm/min, thereby requiring minimal manual correction for imaging. The perpendicular thermal drift should stay within the piezo range to circumvent the requirement of a slow re-approach procedure.

To visualize the rapid growth processes involved, one needs to scan at high-speed, typically an image within seconds would be desirable, possibly even faster.

In order to reduce the dwell time between deposition and imaging, a fast sample transfer is required to minimize the time between geometrically separated PLD position and AFM imaging. The repositioning error for subsequent back and forth motions has to stay below 100 nm.

The requirements can be summarized as follows:

- *Pressures during imaging:* Ranging from 10^{-6} mbar (vacuum) up to 10^{-1} mbar in background gasses of (a mixture of) oxygen, argon and/or nitrogen.
- *Temperature range for imaging:* RT up to 700°C.
- *Imaging resolution:* step resolution at oxide substrates (<0.4 nm) at all mentioned pressure and temperature conditions.
- *Imaging rate:* on the order of (tens of) seconds per image of 256×256 pixels with images of about $1 \times 1 \mu\text{m}^2$.
- *Thermal drift:* below 700 nm/h in perpendicular direction, below 50 nm/min in-plane.
- *Transfer time before and after imaging:* transfer time back and forth within 0.5 s with a repositioning error below 100 nm.

IV. DESIGN

In this section, the general architecture of the vacuum setup, the designed *in-situ* AFM within a PLD vacuum chamber and the design of the AFM scanhead is described in detail.

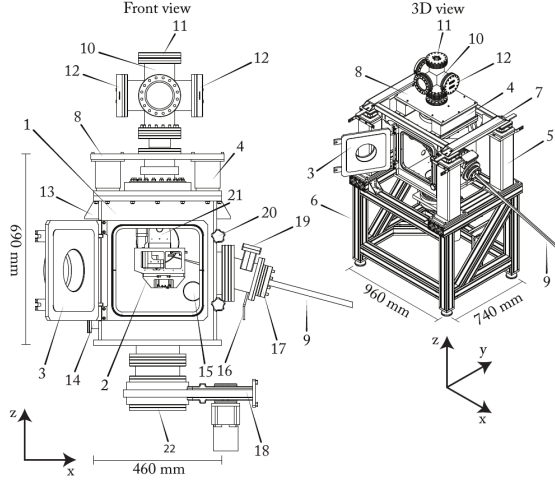


FIG. 2. Schematic drawing of the vacuum setup and peripheral equipment. 1) PLD vacuum chamber, 2) AFM-PLD frame, 3) door of chamber, 4) Halcyonics MOD2-S active damping control element, 5) air damped pods, 6) Aluminum profile system, 7) passive damping stage, 8) active damping stage, 9) incoming beampath for the excimer laser, 10) DN100CF five-way cross, 11) fiber feedthrough, 12) electrical feedthrough, 13) mounting of the passive damping stage, 14) and 15) DN40CF flanges for pressure sensors, 16) gasinlet, 17) DN63CF flange with quartz glass, 18) adaptive pressure controlled valve, 19) valve for laser energy measurement, 20) closing unit door, 21) Aluminum tube for feedthrough and connecting the active damping stage with the supporting frame, 22) DN200CF flange towards turbopump.

A. Vacuum chamber and peripheral equipment

Fig. 2 shows a schematic representation of the designed PLD chamber and peripheral equipment. The PLD chamber is a single vacuum system, which differs in shape compared to traditional cylindrical chambers. In the designed vacuum system, the base pressure of 10^{-7} mbar is limited by O-rings of the vacuum door, valve on the flange on the laser beam path and the pressure controlled valve. Typical PLD background pressures of 10^{-6} - 1 mbar are measured by almost closing this valve and varying the incoming gas flow between zero and 100 ml/min. The vacuum chamber is a square-like box design such that a vacuum chamber door is used to open up the system for accessibility to install the supporting frame for AFM and deposition. The vacuum door has a DN100CF flange viewport window, revolves by a shaft and can be closed by two closing knobs. Four airpod damping units together with matted corks placed underneath provide passive damping of system resonances validated by measuring the transfer function in x- and y-direction²⁶. The vacuum chamber houses an aluminum tube connecting the active damped system towards the supporting frame for AFM and deposition. The active damping stage is mounted as a lid on this PLD chamber ensuring good vibration isolation.

On top of the active damping stage, a five-way cross has been assembled providing feedthroughs for optical and electrical signals from and to the AFM scanner,

coarse approach stepper motor, slider piezomotor drive and heater. The DN40CF flange ports are used for vacuum pressure gauges to measure both, process pressures as well as (high) vacuum pressures.

A KrF excimer laser beam aligned to an optical rail is integrated such that a 248 nm pulsed laser beam, having a typical pulse duration of 25 ns, is focused on the PLD target. As an entrance flange for the PLD excimer laser light, a flange is designed to enable the alignment of the laser onto the PLD target in an angle of 15° parallel to the targets surface. The flange is integrated with a valve to support laser intensity measurements behind the quartz window as well as a gasinlet for the applied background gasses. A flow meter controlled gas manifold has been designed to separately let (a mixture) of nitrogen, oxygen and/or argon into the vacuum chamber through this gas-inlet. At the bottom of the vacuum chamber, a DN200CF flange is connected to an adjustable valve typically used for automated pressure control followed by a turbomolecular pump.

B. Support frame for microscopy and deposition

Fig. 3, schematically illustrates the supporting frame which contains the AFM and deposition stage. This aluminum frame, exhibiting a robust and high stiffness design, is attached by an aluminum tube to an active damping stage, see also Fig. 2. This damping stage has the functionality to lower the vibrational level in the mechanical loop of the AFM. The chosen shape and size of the support frame is based on required sizes and shape of the AFM scanner, PLD deposition and highest mechanical stiffness such that the required vibrational level is not exceeded. The aluminum frame consists of two assembled frames, where the top frame is used for integration of both the AFM scanner and PLD target. The z-approach stage, containing a stepper motor having a step resolution of 100 nm/step, is positioned in the top frame to provide coarse approach towards the sample. A homebuilt mounting bracket connects the coarse approach stage to the AFM scanhead. The PLD target can be mounted onto a holder, adjustable in both height and lateral position along the sample transfer direction. In this design, the distance between the AFM tip and center of the PLD target is typically 50-60 mm, where the PLD target is shielded by a plasmascreen from the AFM scanhead.

The bottom frame has the functionality to integrate a sample transfer stage enabling back and forth sample transfer between the geometrically separated AFM and deposition stage. A vacuum piezomotor with low vibrational level, a repositioning resolution within 20 nm and a maximum speed of 244 mm/s is installed in the bottom frame in order to propel the sample transfer stage which is designed to have minimal mass.

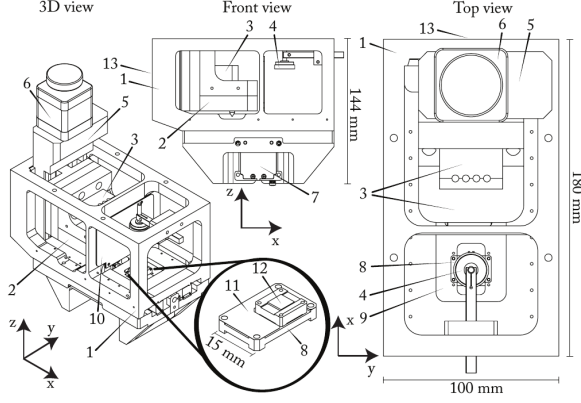


FIG. 3. Schematic drawing of support frame including AFM and PLD. 1) Al frame, 2) AFM flexure scanner, 3) mounting bracket, 4) PLD target 5) coarse approach stage, 6) Vexta 5 phase stepper motor PK545-B, 7) HR4 nanomotion ultrasonic piezomotor, 8) macor heater stage, 9) sample transfer stage, 10) plasma screen, 11) two Kamet HDA pt200 RTD's connected in serie, 12) $5 \times 5 \text{ mm}^2$ sample on top of an $5 \times 5 \text{ mm}^2$ Pt plate and 13) location of screwed cube for integration of acceleration level sensors.

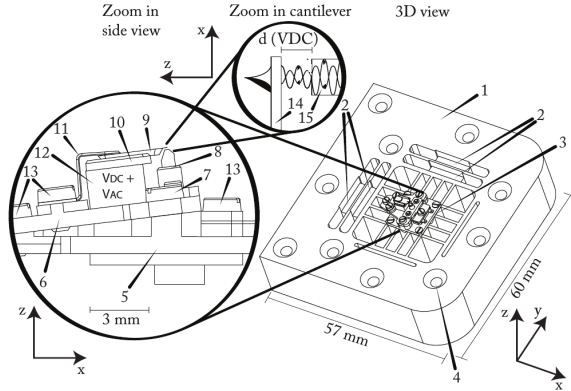


FIG. 4. Schematic drawing of the high resonance frequency AFM flexure scanner, with 1) the Ti6Al4V flexure, 2) stacked XY piezo actuators, 3) AFM chip holder, 4) screw holes, The insets shows the: 5) connection plate between AFM chip base plate and the flexure, 6) cantilever base plate 7) electrical contacts of the dither piezo, 8) ferrule, 9) cantilever chip, 10) chip holder, 11) cantilever clamping spring, 12) dither piezo stack, 13) screws, 14) AFM cantilever, 15) optical fiber end.

C. AFM flexure scanner

The AFM scanner is based on a flexure, see Fig. 4, which is often used in the field of high speed AFM²⁴. Flexure scanners are used as an alternative to commonly used low resonance frequency piezotubes to extend the mechanical scanner bandwidth several orders of magnitude into the kHz range²⁷. In addition, stacked piezo's integrated in a flexure results in less cross-coupling, hysteresis and creep as compared to generally used piezotubes. The AFM flexure in this work has been made out of Ti6Al4V to achieve high stiffness, a resulting high resonance frequency and low thermal expansion in order

to minimize thermal drift. A simulation using finite element analysis resulted in a lowest resonance of 19 kHz for the flexure in the XY-plane. The maximum achievable linerate, estimated as 1/100th - 1/10th of the lowest resonance frequency²⁷, is therefore between 0.19 - 1.9 kHz for this scanner design.

In order to achieve the desired scan range, we make use of piezo actuators with an expansion up to $4 \mu\text{m}$, which strongly reduces up to $1.4 \mu\text{m}$ due to the high preload. The Z-flexure, a piezoring with an effective scan range of $1.4 \mu\text{m}$ is aligned nearly in the center of the XY-flexure and can be positioned with high precision within the XY-plane by the double stacked XY-actuators. A counterbalance piezo, integrated in the Z-flexure, counters the momentum generated by center of mass movement of the Z-piezo. The unit, holding the AFM chip, is displaced by this Z-piezo such that the actual cantilever is excited, see the inset in Fig. 4.

The bottom part of this unit is screwed on top of the Z-flexure and is milled under an angle of 7° . On top of this a flat plate with dither piezo stack is mounted. To detect the cantilevers deflection we make use of optical interferometry through the ZrO_2 ferrule shown in Fig. 4 instead of the more common optical beam deflection method. Beam deflection requires use and adjustment of optical instrumentation, such as mirrors and is impractical under PLD conditions, where space is lacking. Therefore, usage of interferometric detection results in a more compact design. A laser beam is reflected from the cantilever top side and fiber-air interface, where the cantilever and fiber are separated by 40-50 nm. A reference wave is reflected by the planar end of the fiber (glass-air interface). The detected wave is reflected by the top face of the cantilever. Both light waves interfere on a photodiode for detection. The optimal interference working point distance of the cavity can be adjusted by a DC voltage over the dither piezo. On top of this V_{DC} , an AC voltage (typically $V_{\text{AC}} = 1 \text{ mV} - 1 \text{ V}$) is applied to oscillate the cantilever at its resonance frequency f_0 in dynamic mode AFM.

V. PERFORMANCE

In this section we demonstrate the performance of the crucial components of the experimental setup. We focus here on the vibrational level and characteristics of the setup under PLD conditions. We then turn to the imaging performance by demonstrating the imaging of a typical oxide surface, $\text{SrTiO}_3(001)$, under some typical conditions experienced in a PLD experiment as well as the imaging of the growth of a BiFeO_3 film under its PLD growth conditions.

A. Vibrational level and stage translation

Fig. 5 shows the X,Y,Z acceleration levels of the AFM-PLD setup operating at 0.1 mbar oxygen background pressure in comparison to that of the acceleration levels of a commercial AFM setup (Bruker Dimension Icon) op-

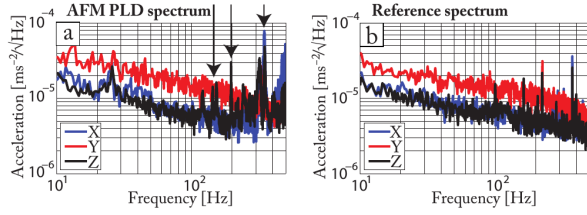


FIG. 5. Vibrational spectra of the, (a) designed setup at a typical oxygen PLD pressure of 10^{-1} mbar O_2 in comparison to a commercial (b) AFM setup. The peaks marked by arrow correspond to resonance frequencies of the aluminum support frame.

erating in ambient conditions. Both systems are placed on the same VC-G classified floor. The vibrational level sensors are positioned in the mechanical loop from tip to the sample, see Fig. 3. The passive damping system suppresses the higher frequencies ≥ 100 Hz, whereas the active damping stage significantly decreases acceleration levels from 10 - 100 Hz. Damping of the system by the airpods is mainly done in the Z-direction. There is no significant influence in acceleration levels observed for the peripheral equipment. Acceleration levels of the designed setup are similar to the commercial AFM setup, see Fig. 5. Only resonance frequencies of the aluminum support frame, see Fig. 2, are found at 140, 190 and several peaks between 300 - 400 Hz, marked by arrows in Fig. 5.

Crucial for the designed setup, is the performance (directly) after stage transfer. We therefore recorded the time domain signal together with the acceleration levels during such transfer. The vibrational decay time of the mechanical AFM tip-sample loop is determined from the time domain signal from the moment that the transfer stage velocity is zero at the AFM position after sample transfer from PLD position to the AFM position, for more details we refer to our earlier report²⁵. In the parallel acceleration level measurements, resonance peaks are observed at 140 and 280 Hz directly after stage deceleration and a corresponding delay time of 0.4 s. The back and forth sample transfer between AFM and PLD is possible in 0.5 s driving at maximum acceleration and velocity.

B. The role of PLD conditions

Typical PLD conditions involve substrates at elevated temperatures and process pressures up to several mbar, a pressure regime where cantilever response is known to alter dramatically²⁸. The cantilever resonance frequency f_0 and the cantilever quality Q factor are nearly constant at pressures ranging from 10^{-6} - 0.1 mbar²⁹. However, Q increases from a few hundred to tens of thousands in the pressure regime 1 bar - 0.1 mbar²⁸, corresponding to a broadening in its frequency response.

Also the elevated substrate temperatures involved in PLD growth, can result in temperature variations of the cantilever during stage transfer. These temperature variations are known to result in unwanted drift of the eigen

frequency f_0 of the cantilever as the cantilevers dimensions alter and the Young's modulus of silicon is known to vary reasonably upon temperature. Measuring f_0 at RT and within close vicinity of a sample heated up to 600°C at a process pressure of 10^{-1} mbar resulted in a frequency shift Δf of 200 Hz, corresponding to a temperature increase of the cantilever of ≈ 70 °C. By use of cantilevers with reasonable but rather low Q factors, the used side-approach¹⁸ upon stage transfer can still be made successful, having the compromise of lower resolution. By the use of a radiation shield we prevented thermal radiation to influence the working point distance of the interferometric setup

C. AFM imaging

In order to demonstrate the scan speed performance we performed tapping mode (TM)-AFM measurements in air, shown in Fig. 6. The scan speed is increased for figures Fig. 6 (a-c) measuring the $SrTiO_3(001)$ substrate steps of 0.4 nm in height. At conventional AFM scan speeds, having a 2 Hz line rate (corresponding to an acquisition time of 256 s/frame), the subnanometer $SrTiO_3$ substrate steps are clearly resolved, see also the height profiles in Fig. 6. From this line-profile, a peak-to-peak RMS of <0.1 nm was found. Upon reducing the acquisition time, see Fig. 6(b) and (c), towards respectively 39 s/frame and 20 s/frame, this peak-to-peak RMS increases towards ≈ 0.3 nm. In addition, a resonance frequency of 1.6 kHz is appearing, a vibrational mode of the mounting bracket connection with the coarse approach stage.

The increase in peak-to-peak z-noise can be attributed to two sources; firstly the electronic noise which increases proportional to $\sqrt{f_{bw}}$, note that the used electronics are known to deliver sufficient resolution at video rate and beyond²⁰. Secondly, the currently used photodetector which is limited to 400 kHz, thereby practically limiting to cantilevers of ~ 300 kHz. A reduced pixel dwell time results in less oscillations used to determine a RMS value for every single pixel.

Typical PLD conditions involve process pressures ranging from high vacuum conditions up to 1 mbar. To demonstrate the use of the microscope at these conditions, in Fig. 7 we show AFM images recorded under typical PLD conditions. In Fig. 7(a), a frequency-modulated (FM) AFM image is depicted of a $SrTiO_3(001)$ substrate containing unit cell vacancy islands of 0.4 nm deep recorded in a background pressure of 10^{-6} mbar at RT³⁰. In this pressure regime, the FM-AFM imaging mode is typically used due to the high Q for image stability reasons and lower transient time compared to TM-AFM^{31,32}. In this FM-AFM image, the vertical resolution is similar to the z-noise level (<0.1 nm) and unit cell (0.4 nm) deep vacancy islands are resolved having lateral sizes of ≈ 20 nm.

In Fig. 7(b), a TM-AFM image is depicted of a $SrTiO_3(001)$ substrate at 10^{-1} mbar oxygen background pressure, which is a typical PLD pressure to deposit perovskite oxide films ensuring good crystal quality, prop-

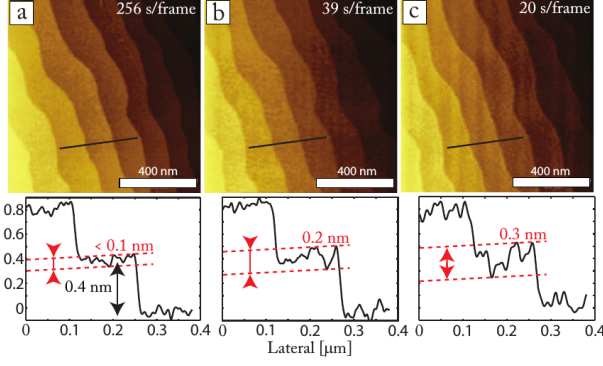


FIG. 6. (Color online) TM-AFM $1 \times 1 \mu\text{m}^2$ 512×512 pixels² images of a SrTiO₃(001) substrate in air at RT with in the bottom panels the corresponding height profiles. The scan speed is (a) 256 s/frame, (b) 39 s/frame and (c) 20 s/frame. The resolution decreases significantly at a scan speed of 20 s/frame due to the limitation of the used cantilever resonance frequency f_0 .

erties, stoichiometric transfer and 2D growth³³. At 10^{-1} mbar oxygen background pressure, the free cantilever amplitude was set to ~ 120 nm and is found to be the most critical parameter for AFM imaging. The lateral AFM resolution on terraces is lowered as a SrTiO₃(001) step broadening of ≈ 20 nm is found at this pressure. An average in-plane drift of 2 nm/min is measured over a period of 3.5 hours under these conditions.

The same AFM settings have been used for a sample measured at $T=600^\circ\text{C}$. At pressures of 10^{-1} mbar oxygen and sample temperatures of $T=600^\circ\text{C}$ vacancy islands can easily be resolved. The AFM noise increase due to temperature is negligible based on the fact that z-noise level and SrTiO₃(001) step broadening remained at $T=600^\circ\text{C}$ ¹⁹. Under these conditions, a drift of 15 nm/min is measured as depicted in Fig. 7. After hours of stable AFM imaging under oxide PLD conditions, the z-piezo stayed within range (± 700 nm).

D. AFM imaging during and after PLD

BiFeO₃ has been deposited as a prototypical ABO₃ film using the described PLD system. This material has multiferroic properties and its growth and property relation is intensively studied^{34–38}. It is reported that BiFeO₃ tends to grow in several types of domains by modifying the SrTiO₃(001) termination³⁸. Dependent on the substrate termination, BiFeO₃ grows either 1D/2D or 3D. Here, BiFeO₃ films have been grown on TiO₂ terminated SrTiO₃(001) substrates anticipating 3D growth. BiFeO₃ was deposited with a laser fluence of 2.0 J/cm^2 , 0.3 mbar oxygen background pressure, a sample temperature of $600\text{--}670^\circ\text{C}$ during deposition and a repetition rate $f_{\text{rep}}=0.5$ Hz, all settings similar to previous work where only a target-substrate distance of 45 mm is used instead of 55 mm³⁸. Fig. 8 shows AFM images obtained after and during BiFeO₃ deposition. In Fig. 8(a), an ex-situ AFM image is depicted of a BiFeO₃ film after deposition of 1000 pulses at 670°C with a film thickness of $\approx 3\text{--}4$ nm.

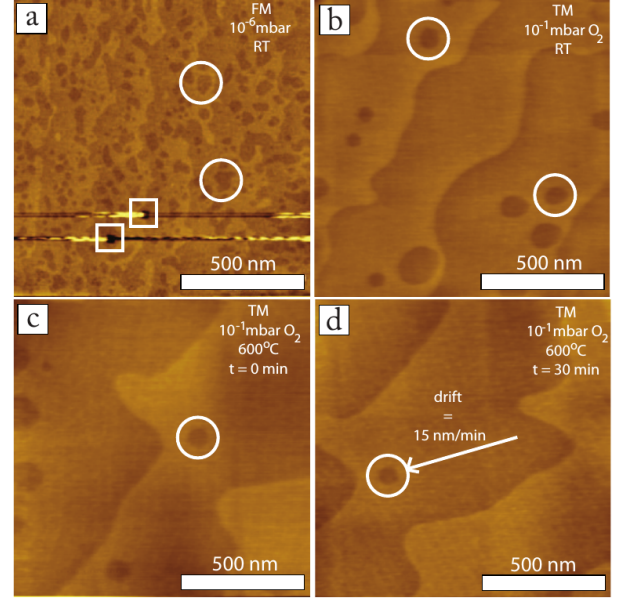


FIG. 7. (Color online) In situ AFM $1.2 \times 1.2 \mu\text{m}^2$ (512×512 pixels²) images of SrTiO₃(001) substrates under different conditions (and different miscut angles) recorded with an acquisition time of 256 s/frame. a) FM-AFM image, $\Delta f = -28$ Hz, $A_{\text{osc}} = 10$ nm, at RT and $P = 10^{-6}$ mbar, b) TM-AFM image, $A_{\text{osc}} = 44$ nm, at RT and $P_{\text{O}_2} = 10^{-1}$ mbar, c) TM-AFM image, $A_{\text{osc}} = 44$ nm, at $T = 600^\circ\text{C}$ and $P_{\text{O}_2} = 10^{-1}$ mbar O₂, d) TM-AFM image, $A_{\text{osc}} = 44$ nm, at $T = 600^\circ\text{C}$ and $P_{\text{O}_2} = 10^{-1}$ mbar O₂ after 30 min AFM imaging. Circle markers surround unit cell vacancy islands with a depth of 0.4 nm and square markers surround etch pits of several unit cells deep.

This BiFeO₃ film was deposited as a reference to reported literature³⁸. It is reported that BiFeO₃ grows 3D on TiO₂ terminated SrTiO₃(001), which is similar to the results obtained here. Terraces with on top 3D islands are visible after 1000 PLD pulses of BiFeO₃ deposited on TiO₂ terminated SrTiO₃(001). The 3D BiFeO₃ islands on top of the terraces suggest that next layer nucleation starts before a previous layer is completely covered. Island step heights are found of 0.2 nm, 0.4 nm and its multiples up to a maximum peak-to-peak height of 3 nm. Islands of 25–30 nm in lateral size are obtained on top of random shaped islands. From these results, it is expected that BiFeO₃ growth will continue 3D, similar to what has been reported³⁸.

In Fig. 8(b), an in-situ AFM image is presented, which was recorded at $T=600^\circ\text{C}$, as this is the maximum stable operating temperature for AFM measurements. The process pressure used was 0.3 mbar oxygen background pressure depositing again 1000 pulses of BiFeO₃. The AFM image was taken after BiFeO₃ deposition, sample transfer from PLD to AFM and an AFM stabilization time of 2h at the AFM position. After thermal stabilization, AFM was started with similar settings used for imaging of a SrTiO₃(001) substrate. It became clear that due to an increase in surface roughness after deposition, the integral gain of AFM electronic feedback had to be increased significantly to visualize the smallest BiFeO₃ islands. Stable AFM imaging was continued for

several hours on BiFeO₃ without thermally drifting out of the z-range. Thermal drift causes small distortions at AFM image edges. Smallest lateral BiFeO₃ island sizes of 20-30 nm have been measured, similar to the results obtained with an ex-situ AFM on BiFeO₃ after deposition at $T=670^\circ\text{C}$ ³⁸. Some of these small islands are surrounded by a white circle marker in Fig. 8. In Fig. 8(b), the square white marker represents a zoom-in of a BiFeO₃ taken from an $0.8 \times 0.8 \mu\text{m}^2$ AFM image.

Afterwards, the BiFeO₃ film grown on SrTiO₃(001) at $T=600^\circ\text{C}$ had a cooldown of $\approx 15^\circ\text{C}/\text{min}$ in its deposition pressure of 0.3 mbar oxygen background pressure. Once the sample reached RT, it was exposed to a maximum oxygen flow up to atmospheric pressure. In Fig. 8(c), an ex-situ AFM image is depicted of BiFeO₃ after oxygen exposure up to atmospheric pressure. The AFM image in Fig. 8(c) is slightly different compared to Fig. 8(b). One difference is that BiFeO₃ islands of $\approx 20\text{-}30$ nm are hardly visible in the ex-situ AFM image, see Fig. 8(c). Both AFM images have in common that BiFeO₃ islands within polygon markers are similar in size. Note that, Q decreases more than an order of magnitude from 10^{-1} mbar background pressure up to atmospheric pressure.

This study reveals that BiFeO₃ can be imaged using a Si AFM tip at $T=600^\circ\text{C}$ and 0.3 mbar process pressure after deposition on a TiO₂ terminated SrTiO₃(001) substrate. Neck formation has not been observed using this tip-sample combination under these conditions. One of the ideas is to deposit BiFeO₃ on mixed terminated SrTiO₃(001) in order to study growth (front evolution) differences on both SrO and TiO₂ termination. However, AFM imaging (Si tip) on mixed terminated SrTiO₃ substrates results in neck formation at $T=600^\circ\text{C}$ and 0.1 mbar process pressure, while stable AFM imaging was achieved on a TiO₂ deposited film on TiO₂ terminated SrTiO₃(001) under the mentioned conditions. From the described measurements and the neck formation of a Si AFM tip with a SrRuO₃ film (SrO termination) at $T=600^\circ\text{C}$ and 0.1 mbar oxygen background pressure, it seems plausible to argue that a Si AFM tip forms a neck if the surface contains a SrO top layer^{19,39}. For this tip-sample combination, another tip material/tip coating needs to be selected.

VI. CONCLUSIONS AND OUTLOOK

To visualize the topography of thin oxide films during growth, we have designed and integrated an atomic force microscope (AFM) in a pulsed laser deposition (PLD) vacuum setup. The in-situ microscope is demonstrated to operate at typical PLD conditions, thereby resolving unit cell height surface steps and surface topography.

We end this paper by discussing some aspects that might improve the performance of this microscope. The setup described here is a major step towards real-time AFM during PLD conditions. To enable quasi real-time AFM monitoring of island growth during PLD, the bandwidth of both the cantilever and (optical) detection system need to be improved, as the acquisition rate is cur-

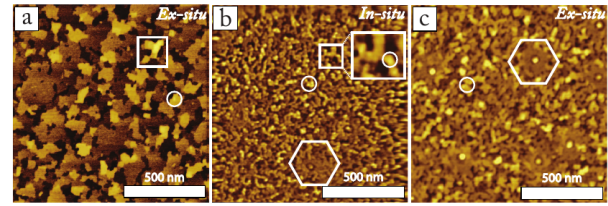


FIG. 8. (Color online) Fig. 3.13 TM-AFM $1.2 \times 1.2 \mu\text{m}^2$ (512×512 pixels²) images, acquisition time=256 s/frame, after 1000 pulses of BiFeO₃ deposited on SrTiO₃(001) (a) ex-situ at RT and in air after deposition at $T=670^\circ\text{C}$, (b) in-situ at $T=600^\circ\text{C}$ and $P_{\text{O}_2}=0.3$ mbar O₂ after 1000 pulses of BiFeO₃ deposited on SrTiO₃(001), (c) ex-situ at RT and in air after deposition at $T=600^\circ\text{C}$. Square markers point to 3D BiFeO₃ islands, circle markers point to small BiFeO₃ islands and polygon markers point to larger islands.

rently limited by them. As high resonance cantilevers dictate smaller physical dimensions on the cantilever itself, the optical detection system might also need reconsideration. We are in the process of the development of self-sensing piezo-electric cantilevers in order to increase the bandwidth by (an) order(s) of magnitude.

Besides this, the thermal drift of the cantilever resulting from varying temperature gradients during sample transfer also needs reconsideration as slight temperature variations of the cantilever might result in a considerable eigenfrequency shift of it. Moreover, increasing both the AFM feedback bandwidth and transfer stage speed will result in a faster tip-sample approach time using the discussed side approach. We therefore currently develop a modification of the geometry such that the temperature of both sample and cantilever is better controlled together with a faster approach.

VII. ACKNOWLEDGEMENT

This work is part of the research programme of NanoNext NL project 9A nanoinspection and characterization, project 07 real-time atomic force microscopy growth monitoring during pulsed laser deposition of oxides.

VIII. REFERENCES

- ¹R. Eason, John Wiley and Sons, Hoboken, U.S.A. (2009).
- ²J. Bednorz and K. Muller, Zeitschrift fuer Physik B Condensed Matter **64**, 189 (1986).
- ³D. Dijkkamp, T. Venkatesan, X. D. Wu, S. A. Shaheen, N. Jisrawi, Y. H. Min-Lee, W. L. McLean, and M. C. P, Applied Physics Letters **51**, 619 (1987).
- ⁴G. J. H. M. Rijnders, G. Koster, D. H. A. Blank, and H. Rogalla, Applied Physics Letters **70**, 1888 (1997).
- ⁵G. Eres, J. Z. Tischler, M. Yoon, B. C. Larson, C. M. Rouleau, D. H. Lowndes, and P. Zschack, Applied Physics Letters **80**, 3379 (2002).
- ⁶J. Neave, B. Joyce, P. Dobson, and N. Norton, Applied Physics A **31**, 1 (1983).
- ⁷T. Shitara, D. D. Vvedensky, M. R. Wilby, J. Zhang, J. H. Neave, and B. A. Joyce, Applied Physics Letters **60**, 1504 (1992).

- ⁸D. Blank, G. Koster, G. Rijnders, E. van Setten, P. Slycke, and H. Rogalla, *Applied Physics A* **69**, S17 (1999).
- ⁹D. H. A. Blank and H. Rogalla, in *Symposium II In Situ Process Diagnostics and Intelligent Materials Processing*, MRS Proceedings, Vol. 502 (1997).
- ¹⁰M. E. Bijlsma, H. Wormeester, D. H. A. Blank, E. Span, A. v. Silfhout, and H. Rogalla, *Phys. Rev. B* **57**, 13418 (1998).
- ¹¹M. Lippmaa, M. Kawasaki, A. Ohtomo, T. Sato, M. Iwatsuki, and H. Koinuma, *Applied Surface Science* **130**, 582 (1998).
- ¹²M. Lippmaa, N. Nakagawa, T. Kinoshita, T. Furumochi, M. Kawasaki, and H. Koinuma, *Physica C Superconductivity* **355**, 196 (2000).
- ¹³K. Iwaya, T. Ohsawa, R. Shimizu, T. Hashizume, and T. Hito-sugi, *Applied Physics Express* **3**, 075701 (2010).
- ¹⁴R. Shimizu, T. Ohsawa, K. Iwaya, S. Shiraki, and T. Hito-sugi, *Crystal Growth & Design* **14**, 1555 (2014).
- ¹⁵G. Binnig, H. Rohrer, C. Gerber, and E. Weibel, *Physical Review Le* **49**, 57 (1982).
- ¹⁶L. Sudheendra, V. Moshnyaga, E. D. Mishina, B. Damaschke, T. Rasing, and K. Samwer, *Physical Review B* **75**, 172407 (2007).
- ¹⁷M. J. Rost, G. J. C. van Baarle, A. J. Katan, W. M. van Spengen, P. Schakel, W. A. van Loo, T. H. Oosterkamp, and J. W. M. Frenken, *Asian Journal of Control* **11**, 110 (2009).
- ¹⁸J. Broekmaat, A. Brinkman, D. H. A. Blank, and G. Rijnders, *Applied Physics Letters* **92**, 043102 (2008).
- ¹⁹J. J. Broekmaat, *In-situ growth monitoring with scanning force microscopy during pulsed laser deposition*, Ph.D. thesis, Enschede (2008).
- ²⁰M. J. Rost, L. Crama, P. Schakel, E. van Tol, G. B. E. M. van Velzen-Williams, C. F. Overgaw, H. ter Horst, H. Dekker, B. Okhuijsen, M. Seynen, A. Vijftigschild, P. Han, A. J. Katan, K. Schoots, R. Schumm, W. van Loo, T. H. Oosterkamp, and J. W. M. Frenken, *Review of Scientific Instruments* **76**, 053710 (2005).
- ²¹N. Kodera, M. Sakashita, and T. Ando, *Review of Scientific Instruments* **77**, 083704 (2006).
- ²²T. Ando, T. Uchihashi, and T. Fukuma, *Progress in Surface Science* **83**, 337 (2008).
- ²³G. Schitter and M. J. Rost, *Materials Today* **11**, 40 (2008).
- ²⁴T. Ando, *Nanotechnology* **23**, 062001 (2012).
- ²⁵W. A. Wessels, J. J. Broekmaat, R. J. L. Beerends, G. Koster, and G. Rijnders, *Review of Scientific Instruments* **84**, 123704 (2013).
- ²⁶F. B. Segerink, J. P. Korterik, and H. L. Offerhaus, *Review of Scientific Instruments* **82**, 065111 (2011).
- ²⁷Y. K. Yong, S. O. R. Moheimani, B. J. Kenton, and K. K. Leang, *Review of Scientific Instruments* **83**, 121101 (2012).
- ²⁸J. Lbbe, M. Temmen, H. Schnieder, and M. Reichling, *Measurement Science and Technology* **22**, 055501 (2011).
- ²⁹J. Mertens, E. Finot, T. Thundat, A. Fabre, M.-H. Nadal, V. Eyraud, and E. Bourillot, *Ultramicroscopy* **97**, 119 (2003).
- ³⁰G. Koster, B. L. Kropman, G. J. H. M. Rijnders, D. H. A. Blank, and H. Rogalla, *Applied Physics Letters* **73**, 2920 (1998).
- ³¹R. Garcia and R. Perez, *Surface Science Reports* **47**, 197 (2002).
- ³²T. R. Albrecht, P. Grtter, D. Horne, and D. Rugar, *Journal of Applied Physics* **69**, 668 (1991).
- ³³R. Groenen, J. Smit, K. Orsel, A. Vailionis, B. Bastiaens, M. Huijben, K. Boller, G. Rijnders, and G. Koster, *APL Materials* **3**, 070701 (2015).
- ³⁴S. H. Lim, M. Murakami, J. H. Yang, S.-Y. Young, J. Hattrick-Simpers, M. Wuttig, L. G. Salamanca-Riba, and I. Takeuchi, *Applied Physics Letters* **92**, 012918 (2008).
- ³⁵H. Ba, B. Ziegler, M. Bibes, A. Barthlmy, and P. Paruch, *Journal of Physics: Condensed Matter* **23**, 142201 (2011).
- ³⁶T. Kanashima, J. M. Park, D. Ricinschi, and M. Okuyama, *Ferroelectrics* **466**, 63 (2014).
- ³⁷N. Deepak, P. Carolan, L. Keeney, P. F. Zhang, M. E. Pemble, and R. W. Whatmore, *Chemistry of Materials* **27**, 6508 (2015).
- ³⁸A. Solmaz, M. Huijben, G. Koster, R. Egoavil, N. Gauquelin, G. V. Tendeloo, J. Verbeeck, B. Noheda, and G. Rijnders, *Advanced Functional Materials* **26**, 2882 (2016).
- ³⁹G. Rijnders, D. H. A. Blank, J. Choi, and C. B. Eom, *Applied Physics Letters* **84**, 505 (2004).